Detection of aerosols in Antarctica from long-range transport of the 2009 australian wildfires

Julien Jumelet, A. R. Klekociuk, Alexander S. P., Slimane Bekki, Alain Hauchecorne, Jean-Paul Vernier, M. Fromm, Philippe Keckhut

DETECTION OF AEROSOLS IN ANTARCTICA FROM LONG-RANGE TRANSPORT OF THE 2009 AUSTRALIAN WILDFIRES

J. Jumelet[1], A. R. Klekociuk[2], S. P. Alexander[2], S. Bekki[1], A. Hauchecorne[1], J.P. Vernier[3], M. Fromm[4], and P. Keckhut[1]

[1] LATMOS CNRS/IPSL UPMC/UVSQ – Paris, France.
[2] Australian Antarctic Division – Kingston, Australia.
[3] NASA Langley Research Center, Hampton, Virginia, US.
[4] Naval Research Laboratory, Washington, US.

Keypoints:

1. First lidar identification of smoke aerosols originating from the 2009 wildfires above the French Antarctic Dumont d'Urville station
2. A dedicated simple microphysical and transport model uses CALIOP data as constraints to successfully model the aerosol overpass above Antarctica
3. Positive ozone anomaly is reported using lidar measurements

Plain Language Summary:

A series of bushfires ignited in the Australian state of Victoria on February 7th 2009 and ended up being the most devastating fire hazard in Australia before the recent 2019/2020 fires. Active remote sensing monitoring instruments are deployed on the French Antarctic station Dumont d'Urville. For the first time, the station recorded presence of aerosols having originated from this biomass burning event at stratospheric altitudes using the atmospheric laser sounding technique (lidar). We combine model calculations to space-borne and ground-based measurements to track the long-range transport of a small filament of the aerosol plume down to the Antarctic station to highlight the possible global impact of such events.

Abstract

We analyze the long-range transport to high latitudes of a smoke particle filament originating from the extra-tropics plume after the Australian wildfires colloquially known as 'Black Saturday' on February 7th 2009 and report the first Antarctic stratospheric lidar characterization of such aerosols. Using a high-resolution transport/microphysical model, we show that the monitoring cloud/aerosol lidar instrument operating at the French Antarctic station Dumont d'Urville (DDU-66°S-140°E) recorded a signature of those aerosols. The 532 nm scattering ratio of this filament is comparable to typical moderate stratospheric volcanic plume, with values between 1.4 and 1.6 on the 1st and 3rd days of March above DDU station at around the 14 and 16 km altitude respectively.

A dedicated model is described and its ability to track down fine optical signatures is validated against Antarctic lidar elastic aerosol and DIAL ozone measurements. Using one month of tropical CALIOP data to support a relatively simple microphysical scheme, we report modeled aerosol presence above DDU station after advection of the aerosol size distribution. In situ measurements also report associated positive ozone anomaly.

This case study provides evidence that biomass burning events injecting significant amounts of material up to stratospheric altitudes can be transported towards high latitudes. We highlight a potential imprint of smoke particles on the Antarctic atmosphere over larger time scales. Any underestimation of the global impact of such deep particle transport will lead to uncertainties in modeling the associated chemical or radiative effects, especially in polar regions where specific microphysical and chemical processes take place.

1. Introduction

Aerosols are known to cause significant effects on the radiative balance of the Earth, both directly, through scattering and absorption of short-wave and long-wave radiation [Charlson et al., 1992], and indirectly, by acting as condensation nuclei [Penner et al., 2001]. As a matter of fact, long-term observations of stratospheric aerosols are needed for understanding the global atmospheric temperature and ozone layer variability [Thomasson and Peter 2006]. The role of particles, being either sulfated background/volcanic aerosols or carbon-based smokes as cloud condensation nuclei, is especially important in Antarctica. Recent studies also tend to demonstrate that polar aerosols can be characterized by large variations in their optical, physical and chemical composition parameters, causing a wide variety of particulate radiative properties throughout the year [Wang et al., 2005; Tomasi et al., 2007]. Besides, Polar Stratospheric Clouds (PSCs) grow from stratospheric sulfate aerosols under given temperature thresholds and have a crucial impact on stratospheric ozone depletion [Adriani et al., 2004; Spinhirne et al., 2005; WMO, 2018], and on radiative balance, which in turn modulate the local circulation [Liou, 1986; Ramanathan et al., 1989; Lachlan-Cope, 2010]. Polar clouds are also involved in the equilibrium of the largest freshwater reservoir in the world [Arthern et al., 2006].

Because of the low aerosol number concentration, their direct effect was first thought to be negligible in Antarctic regions [Bodhaine, 1995]. But, above snow- or ice-covered areas, multiple scattering between these particles, cloud surface, and ground surface may still lead to some degree of warming [Randles et al., 2004; Liu et al., 2013]. Aside from the background sulfate aerosols, smoke particles also act as nucleation sites, favoring the growth of sulphuric acid droplets. Smoke particles also have a greater absorption/heating potential than sulfate particles [Burton et al. 2012, Weller et al., 2013]. Therefore, the global effect of a given stratospheric aerosol load has yet to be precisely estimated as it is as highly dependent on latitude as it is on chemical composition.

Worldwide information on stratospheric aerosols is now available from remote sensing instruments, especially with the numerous space missions [SPARC, 2006]. Nevertheless, the Antarctic particle budget remains hard to monitor due to an evident lack of instrumental capabilities beside the sparse ground stations which are mainly located at the edge of the continent. Pollution originating from trans-continental transport is increasing at high latitudes [Stohl and Sodemann, 2010]. Bullard et al. [2016] highlighted the significant impact of dust event and processes at high latitudes. Antarctica is more isolated from human activities than the Arctic and this geographical situation results in a lower density of aerosol particles relative to other regions [Ito, 1986].

Exchanges between troposphere and stratosphere have important impacts on atmospheric chemistry by mixing air masses containing potent greenhouse gases like ozone and water vapor [Gauss et al., 2003; Forster et al., 2007] and by air masses from lower latitudes entering the Antarctic circulation. Particle sedimentation and aerosol deposition then cause ice cores to act as climate proxies keeping track of past aerosol concentration levels [Wolff and Peel, 1985; McConnell et al., 2007]. Ice core samplings may also contain information on the frequency and intensity of past volcanic eruptions [Sigl et al., 2014]. Around 1.5% of stratospheric air reaches the surface after 10 days which is around the average age of air mass at the ground level in spring [Stohl and Sodemann, 2010]. However, the extent, scales and impact (either volcanic or biomass burning) occurring at lower latitudes on the Antarctic atmosphere through deep transport is still unclear. The particular processes taking place in Antarctica make the assessment of this impact a critical point in the interplaying interactions between ozone and climate [WMO, 2018].

This case study reports evidence of another source of stratospheric Antarctic aerosols related to biomass burning. Biomass burning may spread across large areas and significantly increase temperature and generate some explosive troposphere to stratosphere transport favored by intense forest fire. Convective processes associated with fire activity are referred to as pyroconvection and under specific heat and moisture conditions, fire-generated aerosol release can lead to thunderstorm-like convective cloud known as PyroCumulonimbus (PyroCb). This feature has been reported and investigated, with many events spanning from 1950 up to now [Livesey et al., 2004; Waibel et al., 1999; Fromm et al., 2000, 2005 ; Siebert et al., 2000 ; Fromm and Servranckx, 2003 ; Jost et al., 2004 ; Tupper et al., 2005 ; Fromm et al.; 2006, 2008 ; Peterson et al., 2015; Kablick et al., 2018]. One of the interesting features of the PyroCb events is that the microphysics and dynamics of associated plumes are most often very close to characteristics observed in the case of volcanic eruption [Peterson et al.,

2018]. Modeling studies have shown that tropospheric plumes above thunderstorms are very likely to enter the lower stratosphere, from which they may reach latitudes far removed from their emission location [Wang, 2003]. In the case of an underestimated frequency of such events, this process could be considered a new alternative to efficiently redistribute gases throughout the Upper Troposphere / Lower Stratosphere range (UTLS). While it is an efficient source process to inject particles up into the stratosphere, further studies are still required to better identify the convective storms responsible for this injection, with both observations and modeling required [Fromm et al., 2005]. In terms of optical measurement analysis, this also questions any misleading attribution of such carbonated aerosol signatures to volcanic activity. Discrimination of aerosols as of either volcanic or biomass burning origin requires microphysical information that can be provided by highly sensitive measurement capabilities such as those of lidar instruments.

The transport of material over long distances, and especially smoke, is not often directly observed in the Antarctic UTLS. A few individual events have been documented, such as the transport of dust from Patagonia [Gassó et al., 2010] or smoke from biomass burning in South America [Evangelista et al., 2007; Pereira et al., 2006] to the tip of the Antarctic Peninsula. Fiebig et al. [2009] revealed transport of biomass burning aerosol from South America to an inland site on Queen Maud Land. Statistical studies of transport down to Antarctica have also been performed using trajectory calculations for single measurement stations or ice core drilling sites [Kottmeier and Fay, 1998]. Weller et al. [2013] investigated seasonal variations of black-carbon particles and albedo assessment with a maximum variability in spring time from decadal time series using absorption photometers. However, microphysical modeling and transport of particles from the lower latitudes down to Antarctica remains difficult due to scale issues within the models: large scale is needed for longer runs and small scale resolution needed to resolve the numerous fine filaments. Models have often been used in conjunction with ground-based measurements to attribute pollution in Antarctica to its sources [Stohl and Sodemann, 2010]. As for ground-based detection, the lidar instrument still remains one of the best suited to monitor and detect small changes in particle load in the UTLS, with a vertical resolution often under 100m and very high sampling frequency.

This paper reports observations along with microphysical and transport simulation of a specific smoke filament originating from the particle plume which was largely confined within the tropics one month after the Australian bushfires. The overall complex structure of the different plume layers has been used as an additional constraint in our model both upon initialization and during the simulation we present here. We describe a methodology based on a combination of local and global lidar measurements along with a simple coupling of optical and transport modeling. We aim at taking advantage of local measurements to efficiently report on similar fine events (or those involving long range transport of volcanic aerosols). We also highlight the importance in having ground reference monitoring measurement stations to complement and validate global measurements, model results or even to some extent microphysical schemes through case studies like this one. Section 2 provides additional information on the event. Observations and numerical tools are described in section 3. Section 4 details the transport method and simulation setup. Section 5 discusses the model results against observations before drawing conclusions in section 6.

2. The 2009 Australian Bushfires

2.1. Event Description

In the Southern Hemisphere, biomass burning activity is minimal in February. The major fire sources of Indonesia, Africa and South America become significant later in the year [Edwards et al., 2006]. Particle transport from these areas has a strong seasonality with maxima in winter for Southern Africa and spring from South America and Australia [Stohl and Sodemann, 2010]. A series of bushfires ignited in the Australian state of Victoria on February 7th 2009 and ended up being the most devastating fire hazard in Australia up to the recent 2019/2020 event and are now referred to as the 'Black Saturday' bushfires. Over 4500 km² of land burned to ashes, and more than 170 fatalities were recorded with major fire spots identified over 2 weeks from the Black Saturday [BOM, 2009]. The intensity of the Victorian bushfires was such that pyroconvection uplifted gas species along with particles up to stratospheric altitudes. Such typical transport of gas and particles has been reported by Wang [2003], Fromm et al. [2005] and Field et al.[2016]. On 'Black Saturday', the combination of typical meteorological synoptic features with lack of precipitation and localized convective processes rose the fire danger level to extreme and several PyroCb were identified [Reeder et al., 2015; Tosca et al., 2015; Field et al., 2016]. Recent investigations of the responses between the fires and the atmosphere lead to a better understanding of the pyroconvection processes and especially the risk of new fire ignitions using pyrogenic lightning. Dowdy et al. [2017] gathered evidence of pyroconvection in the Black Saturday events using a number of distinct electrified PyroCb clusters, therefore retro-validating the studies on the deep imprint of these plumes on the Southern Hemisphere atmosphere during several months [Siddaway and Peletina, 2011; Pumphrey et al., 2011; Glatthor et al., 2013].

The main smoke plume was first observed at stratospheric altitudes the day after the outbreak and encircled the globe approximately 6 weeks after being first detected [Pumphrey et al., 2011]. Similar to typical volcanic behaviour, smoke aerosols remained in the extratropical channel. From mid-February to June, it was mostly located between 18-22 km altitudes (see Section 5). Space-borne observations acquired onboard the CALIPSO satellite reported both the main part of the plume within tropical latitudes and various filaments reaching higher latitudes but backscatter values after 2 or 3 months often reached the lower detection limit of the lidar instrument. Siddaway and Peletina [2011] used OSIRIS observations to report a predominant westward direction in the smoke plume transport and characterized advections from around 19 to 22km up before the end of April, and background radiance levels on OSIRIS observations by mid-June 2009.

3. Observations

3.1. Ground-based lidar

Lidar observations have been carried out at the French station Dumont d'Urville [DDU] (66°S - 140°E), since April 1989 within the framework of a French (LATMOS/IPSL) Italian (ISAC/CNR) cooperation. The station is a primary site of the Network for Detection of Atmospheric Composition Changes (NDACC). Except for year 2000 and 2005, aerosols and PSCs measurements have been routinely carried out at DDU every year since 1989, from roughly mid-March to late September

[David et al., 1998, 2005] providing the only continuous aerosol lidar time series over 30 years in Antarctica. The DDU Rayleigh/Mie lidar was originally designed to operate in two exclusive modes, one for ozone and one for aerosol/PSC and temperature measurements. The ozone mode includes light emission and reception at wavelengths of 308 and 355 nm and additional reception at 332 and 387 nm. The aerosol mode includes emission and reception at wavelengths of 532 and 1064 nm. Lidar measurements are performed at DDU on a yearly winter campaign basis; the main focus being on polar stratospheric clouds monitoring during the winter and early spring months. For calibration purposes and additional aerosol records, a lighter measurement calendar also plans lidar acquisitions from early March, when the sky gets dark enough for the lidar to safely operate for extended measuring sessions. Within the operational frame of the NDACC, some alerts regarding specific events like volcanic eruption and specific air mass intrusions may trigger additional acquisitions.

A complete description of both the instrumental design and inversion procedure is featured in [David et al., 2012]. The Nd:YAG laser source emits 500mJ per pulse at 1064nm at 10 Hz frequency, doubled in frequency to 532 nm. A collocated Excimer laser emits 55 mJ per pulse at 308 nm at 80 Hz frequency. Backscattered signal is collected by an 80 cm telescope. Aerosol vertical density profile is defined as the backscattering ratio or Scattering Ratio (hereafter called SR) expressed as the ratio of extra scattering of aerosols to the molecular scattering of air at the same altitude. After a preprocessing phase removing potential saturation effects and background noise level (low at this time of the year in Antarctica), lidar signals are inverted using the Klett-Fernald formalism [Klett 1981,1985; Fernald, 1984], to derive individual SR profiles. The zero-reference altitude is set between 28 and 32 km depending on signal-to-noise ratio. The extinction-to-backscatter ratio is set to 50 sr which is a commonly assumed value for small aerosol loading and even periods of moderate volcanic eruptions [Ridley et al., 2014]. Cumulative uncertainties of the backscatter measurements induced by random detection processes, possible presence of aerosol at the reference altitude and the error in lidar ratio value do not exceed 10% as reported by Chazette et al., [1995]. Another major source of uncertainty is the molecular number density used in Rayleigh calculations derived from atmospheric pressure and temperature profiles. The lidar inversion is particularly sensitive to the molecular density and the clear-air reference altitude. Collocated radiosondes are used to estimate reference atmospheric density and interpolation and scaling to National Centers for Numerical Prediction (NCEP) daily meteorological data is done at balloon burst altitude.

Ozone profiles are retrieved using the DIfferential Absorption Lidar (DIAL) technique. The ozone number density can be derived from two signals, one being strongly absorbed by ozone (308 nm), the other (355 nm) being only weakly absorbed. The Nd:YAG frequency is tripled to 355 nm to provide the reference signal whereas the Excimer laser directly emits at the 308 nm. Pre-processing of the lidar signal in ozone mode is similar to the aerosol mode. Ozone concentration is retrieved without external assumptions by comparing the number of laser shots between the absorbed and reference wavelengths [David et al., 2012].

To complement the simulations presented in this paper, we also include a lidar profile acquired at the Australian Davis station (-68.6°S, 78°E). The 532nm SR is obtained with the Klett-Fernald formalism after normalization at 30-35km altitude. The molecular signal is derived from density profile

inferred from measurements by the AIRS instrument onboard the Aqua satellite. As for DDU, the lidar ratio of the background aerosol is assumed to be 50 sr. For observations used here, a mechanical chopper reduced signal levels below approximately 11 km altitude. Further details of the system and analysis procedure are provided by Alexander et al. [2011]. Observations were made with the Davis lidar system throughout the autumn during quiescent tropospheric weather, however only data collected on February 26th are relevant for comparisons with the simulations discussed below.

3.2. Satellite aerosol sounders

The CALIOP (Cloud-Aerosol Lidar with Orthogonal Polarization) instrument onboard the CALIPSO satellite platform is a nadir-viewing active sounder [Winker et al., 2010]. Operational since June 2006, CALIOP provides range-resolved measurements of elastic backscatter at 532 nm and 1064 nm with a vertical resolution of around 200 m at stratospheric altitudes. CALIOP lidar makes use of a Nd:YAG laser operating at 20.2 Hz with a 110 mJ/pulse power and a 0.78 m^2 telescope. In this study we use data based on the night-time 532 nm level 2 product, post-processed using a treatment described by Vernier et al. [2009]. We assume backscatter measurement uncertainties around 20% as stated in Winker et al. [2010]. We also use the level 2 Cloud-Aerosol discrimination score to characterize the smoke particles. The CALIOP 532 nm SR is obtained after applying an extinction correction on the attenuated backscatter with a generic non-background regime stratospheric aerosol lidar ratio of 50 sr. We focus on UTLS altitudes, where attenuation is lower than in the lower troposphere, especially from a space-borne acquisition geometry. The molecular atmospheric profile is derived from temperature and pressure provided by Goddard Earth Observing System [Yasunari et al., 2011].

The Atmospheric Chemistry Experiment (ACE) was launched in August 2003 onboard the Canadian scientific satellite SCISAT-I. The high-resolution spectrometer measures during sunrise and sunset infrared absorption to provide vertical profiles of atmospheric compounds (gases and particles). Aerosols and clouds are monitored using the solar radiation extinction measured by two filtered imagers at 527 (VIS) and 1020 nm (NIR) [Dodion et al., 2007]. The satellite operates in a circular orbit at an altitude of 650 km. Aerosol extinction profiles are obtained by subtracting the gas extinction contribution (air, O_3, NO_2) derived from the Fourier Transform spectrometer from the total atmospheric extinction profiles. On average, the NIR ACE imager gives results that are 20% higher than SAGE II instrument [Gilbert et al., 2007].

4. Numerical simulations

4.1 The aerosol microphysical and transport model

The Modèle Isentropique de transport Mésoéchelle de l'Ozone Stratosphérique par Advection (MIMOSA) model [Hauchecorne et al., 2001] is originally a Potential Vorticity (PV) advection model running on isentropic surfaces (surfaces of constant potential temperature). The advection scheme is semi-Lagrangian with a time step of 1 hour. Regridding onto the original orthonormal grid is performed every 6 hours. The model resolution is 0.5°x0.5°. The advection is driven by European Centre for Medium Range Weather Forecast (ECMWF) meteorological analyses at a resolution of 0.5°x0.5°. The accuracy and mass conservation of the model have been evaluated by Hauchecorne et al. [2001] and

validated against airborne lidar ozone measurements using the strong correlation between PV and ozone, a quasi-conserved chemical tracer on a week timescale within most of the lower stratosphere [Heese et al., 2001].

A sectional aerosol microphysical module has been coupled to MIMOSA to simulate the formation, transport and microphysical evolution of stratospheric aerosol particles [Jumelet et al., 2009]. The size distribution is discretized into a number of size bins using a geometrically increasing volume scale. The number of size bins is 50 with the bin particle radius ranging from 0.01 to 5 µm. The model prognostic variables are the number density of each size bin and chemical composition. The module also includes an optical routine that calculates theoretical properties such as volume backscatter and/or extinction coefficients at given wavelengths (in the visible and near-infrared domains e.g. the 532 nm aerosol wavelength) from the model-simulated particle size distribution and the composition-dependent refractive index.

We consider here two different aerosol types within the model, one being the background sulfate stratospheric aerosols and the other one being the injected smoke particles. Since background sulfate aerosols are not relevant to our long-range transport case study, only the results for smoke particles are presented and discussed here. In order to simulate smoke particles, the original aerosol scheme is extended. Smoke particles can be complex objects, i.e. a homogeneous mixing of organic and inorganic aerosol components with black carbon coating in some more or less complex core/shell structure often modelled using fractal aggregates [Smith and Grainger, 2014]. However, our approach is simple because the objective is to calculate the aerosol optical parameters (properties integrated over the entire distribution) instead of the detailed behaviour of the size distribution and the 532nm SR will be driven by observations. Dählkotter et al. [2014] have shown that the optical properties of aged forest fire smokes (having experienced intercontinental transport) can be estimated with Mie Theory without any major uncertainty. The smoke particles are treated here as a mixture of sulfate/black carbon with overall real refractive index at 1.85 [Smith and Grainger, 2014, Mischenko et al., 2014]. The smoke SR is calculated using the Mie scattering code with aspherical aspect ratio at 1.50 [Scarnato et al., 2015]. There are still computational uncertainties in the optical calculations due to the limited number of bins covering the size range that drive the overall uncertainty estimated around 20% on the backscatter coefficient.

4.2 Initialisation & CALIOP SR insertion into the model

The initialization of aerosol size distributions is based on measurements. There was no significant volcanic influence on aerosol loading at the time of the Australian Bushfires in the southern hemisphere. For this reason, the sulfuric acid aerosol size distribution was initialized over the entire model domain with a typical background (non-volcanic) lognormal distribution: N_o=10 cm^{-3}, r_m=0.07 µm and σ=1.8 [Pinnick et al., 1976; Larsen et al., 2000]. To our best knowledge, no information on the Australian smoke particle size distribution are available. The smoke size distribution is therefore initialized with a lognormal distribution based on data collected in the northern hemisphere on a comparable PyroCb particle plume after a similar event of smoke long-range transport (N=50 cm^{-3},

330 r_m=0.12 µm and σ=1.3) [Dahlkötter et al., 2014]. This size distribution can also be typical of the fine
331 mode of volcanic aerosol plumes.
332
333 The initialization of the stratospheric aerosol spatial distribution is based on the insertion of
334 CALIOP SR measurements in the model. The insertion is straightforward as compared to other
335 approaches where CALIOP backscatter products have already been successfully assimilated in several
336 studies using full assimilation schemes [Sekiyama et al., 2010; Campbell et al., 2010]. From a data
337 assimilation point of view, our insertion scheme is equivalent to a sequential assimilation assuming
338 model errors to be much greater than observational errors and using our optical model as
339 observational operator. Our scheme remains local because the insertion of one single observation only
340 impacts one model grid cell, meaning the length-scale of the spatial correlation is taken to be less that
341 a size of a grid cell, i.e. less than 0.5°.
342
343 The insertion procedure is the following: one variable of the aerosol size distribution
344 parameter (the so-called control variable) at each grid cell is modified iteratively in order for the model-
345 calculated SR to match the CALIOP-observed SR. The choice of the control variable depends on the
346 value of the observation, controlling the aerosol type. When CALIOP SR is smaller than the background
347 value (taken as 1.025, from simple Mie Calculations on H_2SO_4/H_2O droplets), one can assume that the
348 measurements correspond to stratospheric sulfuric acid aerosols and the control variable is the total
349 aerosol concentration N. The median radius and standard deviation remain unchanged (r_m=0.12 µm
350 and σ=1.3). Note that, in that case, the optical module uses the aerosol optical index of sulfuric
351 acid/water solution in equilibrium with the gas phase [Jumelet et al., 2009]. When CALIOP SR is greater
352 than 1.025, the measurement is taken as indicative of the presence of smoke particles and the control
353 variable is the mode radius. N and standard deviation remain unchanged. In that case, the optical
354 module uses the smoke refractive index. This choice of control variable for smoke type is based on the
355 fact that there is little information on smoke particle size and, within the range of smoke size
356 distribution parameters, model-calculated SR is assumed to be much more sensitive to the mode
357 radius than to the total number concentration, the latter variable displaying a linear behavior regarding
358 the aerosol backscatter coefficient.
359
360 The first 2 weeks of the simulation in January, before the fire outbreak, define the spin-up
361 phase. In this phase, continuous high-frequency CALIOP SR insertion on the whole grid slowly shifts
362 modelled stratospheric aerosol SR towards CALIOP measurements. After the spin-up, the average
363 aerosol levels do not change much beyond sedimentation, and the model reaches some degree of
364 equilibrium regarding the forcing of satellite observations.
365
366 ### 4.3 Model set-up and simulations
367
368 A key aim of the present study is to test the model ability to forecast the position of plumes
369 of either volcanic or biomass origin. For this reason, simulating these long-range transport events use
370 aerosols as tracers. After the initialization/spin-up phase, CALIOP SR data are inserted in the model
371 during the run, but only outside a large free-running model domain. The CALIOP insertion carries on in
372 order to maintain realistic boundary conditions on this free running domain. The sensitivity of the

model results has been tested by varying the latitude of the free running domain boundary beyond which the aerosol particles are freely advected (no CALIOP SR insertion). Stable results were obtained when the CALIOP insertion is confined to the region equatorward of 50°S latitude. Of course, the CALIOP insertion domain covers the Australian source region. We keep the latitude of the limit between the free running insertion zones relatively low to highlight the efficiency of the transport model.

The model is integrated from January 1st to May 1st, with an advection step of 1 hour, and a regridded output is dumped every 6 hours. The model is run at several isentropic levels every 10 K over the 400-450 K potential temperature range on a southern hemispheric grid. It is forced with ECMWF temperature and pressure fields at a 0.5°x0.5° resolution. The spin-up phase covers the first 2 weeks of January. After that, CALIOP SR data are only inserted outside the large free-running model domain, equatorwards of 50°S. The signature of the Australian fire plumes at stratospheric altitudes is clearly detected after 2 days after the outburst on February 7th above the 410 K level.

5. Results

5.1 CALIOP and lidar observations

Two weeks of 532 nm CALIOP SR averaged data are presented on Figure 1. The figure shows the evolution of smoke plume distribution between February 1st and 16th. Recall that the fires started on February 7th. To avoid any false detection, only SR above 1.1 (clearly indicative in this study of smoke particles) are considered. The SR averaged over the 15-25 km altitude range show the plume in the South Pacific (Figure 1a). The SR vertical distribution as a function of longitude (data averaged over the 25°S-50°S latitudinal band) also confirm the presence of smoke particles in the 15-22 km altitude range (cf. Figure 1b). Figure 1c shows the zonal mean SR distribution (data averaged along latitude circles) with isentropic levels superimposed; smoke particles remain mostly confined between the 380 K and 450 K isentropic levels during the first 2 weeks of February, although an analysis at higher time resolution revealed that few smoke particles can be detected up to the 500 K level a few days after the fire outbreak (not shown).

The plume is identified above DDU station during a short time span in early March, with unambiguous signatures on the 1st and 3rd. At that time, no direct comparison with CALIOP is available. CALIOP data and results of model simulations (described in the next section) indicate more overpasses of the smoke plume above DDU, but no lidar measurements were available due to bad local weather conditions. Both vertical ground-based SR profiles obtained on the 1st (Figure 2a) and 3rd of March (Figure 2b) reveal clear signals of smoke particles at 13-14 and 16-17 km respectively. SR peaks at 410 K and 450 K on the March 1st (Figure 2a) and March 3rd respectively. Note that the lidar data are averaged over ~160 min on March 1st and ~210 min on March 3rd. SR peaks above 1.4 in both cases which is higher than SR signals of minor volcanic eruptions [Vernier et al., 2011]. An additional weaker layer can also be seen just above 15km (Figure 2a). It is worth pointing out that measurements at this time of the year (at the end of continuous Antarctic daylight) were performed for calibration purposes in March, related to nighttime sky conditions.

5.2 Model simulations versus DDU lidar detection

Figure 3a shows the plume filament on February 26th, a few days prior detection above DDU on March 3rd, near the location of the Davis station. Figure 3b shows the associated lidar profile on the same day, with a broad but weak peak of about 1.05 around 20km. This small SR value may be indicative of background aerosols, especially as 2009 is a volcanic quiescent time period. Besides, lidar measurements have been integrated on several hours. Even if the plume position is at the Davis longitude, identification is not clear looking at the lidar profile, especially considering that for small SR values, the molecular scattering derived from the pressure and temperature profiles is a sensitive parameter. Still, aerosol loading is present and there is a strong agreement between Figure 3a and 3b, in that the simulated plume does not reach Davis with scattering ratios greater than 1.1.

Figure 4 shows modeled SR fields between February 10th (Figure 4a) and March 10th (Figure 4i) on the 410 K level corresponding to the altitude of the ground-based SR peak on March 1st. The highest CALIOP SR values are detected during the first half of February, with values peaking slightly above 1.4 and gradually decreasing below the 1.1 threshold during the first half of April (not shown). A weak plume spanning both sides of South America is visible in the modeled SR field in February. This is not related to the Australian fires and will not be discussed here. A week after the fire outbreak, a small patch of high SR values appears on the 10th of February east of Australia (Figure 4a). This patch, indicative of the smoke plume, carries on being transported eastward. At the same time, it is very strongly stretched by wind shear, forming a large filament extending over thousands of kilometers. Filamentary structures quickly form at the subtropical barriers. Between the 20th and 25th of February, the plume filament split into two main parts with the main part remaining in the tropics and a smaller filament being transported towards higher latitudes.

Around the time of the fires and during the ascension between Feb 8th and 16th, part of the CALIOP data may have been misflagged so the overall aerosol load near the tropics may not be accurately depicted. This issue is still out of focus as we aim at identifying the small filament transported at high latitudes and clearly separated from the main bulk (visible from Figure 4d). Besides, the consistency of SR values (excluding high cloud scattering) has been checked prior to integration within the model.

Overall, several smoke plume filaments were observed over a wide altitude range (13-22km) with CALIOP till the end of May. Even though the bulk of the smoke plume did not cross the subtropical barrier, smaller filaments occurred throughout the extratropics due to efficient quasi-horizontal transport (along isentropic surfaces) in the lower stratosphere. After one month of long-range transport, the plume is detected above DDU on the 1st of March during the time of the measurements, between 13:33 and 16:12 UT (see Figure 2). The model indicates the passing of a thin filament just above the station on the same day (see Figure 4f); model outputs are only available every 6 hours. In order to investigate the passing of the filaments above DDU, Figure 5 displays a close-up of the simulation at 410 K and 450 K, respectively on March 1st and 3rd when the DDU lidar clearly detected

458 the plume. There is a reasonably good agreement in terms of timing. The ground-based measurements
459 in Figure 1a and 1b identified 2 layers peaking at 410 K and 450 K. The lower layer is detected on March
460 1st, the higher layer is detected on March 3rd. This is consistent with the model simulation which shows
461 a DDU overpass at 410 K level only on March 1st (Figure 5c) but not on March 3rd (Figure 5d); it is very
462 close to the time of the afternoon lidar plume measurements whereas the model output is set at
463 12:00 UT. The model simulation also appears to be in agreement with the DDU lidar at 450 K level with
464 a DDU overpass only on March 3rd (Figure 5b) but not on March 1rst (Figure 5a).
465
466 As expected, the modeled SR values are in excellent agreement with CALIOP SR. However, the
467 peak modeled SR is slightly higher than the corresponding maximum values of the DDU ground-based
468 lidar. The instantaneous model outputs (every 6 hrs) show the maximum SR values within the smoke
469 filament whereas the ground-based lidar data correspond to around a 3 hr time average of the passing
470 filament as seen from a local atmospheric column above the station. Model fields show that there are
471 sharp SR gradients within the plume. It is unlikely for the ground-based instrument to probe only within
472 the most dense parts of the filament. Furthermore, space-borne and ground-based lidars have
473 different acquisition fields of view and different data processing (calibration, inversion, spatio-
474 temporal averaging), and small discrepancies cannot be ruled out. In view of these caveats, the
475 agreement between the ground-based lidar measurements and the CALIOP-driven model simulation
476 can be viewed as good. It indicates that the setup is able to accurately model long-range transport of
477 the information provided by CALIOP measurements from 50°S (the edge of the free-running model
478 domain) down to Antarctica. This also suggests that the transport scheme and the ERA-Interim winds
479 driving the advection are accurate enough if the model is used as a forecasting tool. After the DDU
480 overpass, during the first 10 days of March, the plume is stretched and breaks into smaller parts that
481 are scattered throughout the extratropics and high latitudes.
482
483
484 **5.3 Model simulations versus ACE measurements**
485 ACE imager measurements of extinction ratio on March 4th were used as a comparison to the
486 modeled SR field. Figure 6. displays the model SR with crosshairs at the location of the ACE
487 measurements. Overall, SR values peak at slightly above 1.6 as forced by CALIOP measurements. The
488 main bulk of the plume remains confined within tropical latitudes, even though the largest SR values
489 are found in a filament crossing out of the tropics at the square location. Figure 7 displays ACE imager
490 measurements of extinction ratio on the same March 4th, when the plume has been clearly identified,
491 peaking respectively at 19 and 21 km. Figure 7b displays associated VIS and NIR imager extinction
492 coefficients. In early March, the total AOD fell to around 0.002 and 0.006 for the NIR and VIS
493 respectively whereas it was estimated around 0.03 in February. Once again, the SR values on Figure 6
494 follow the shape of very fine dynamic structures that can be difficult to model without dedicated
495 microphysics and resolution but a large amount of particles seems to be able to cross the tropics.
496 Burton et al. [2012] provides an assessment of the 532 nm extinction to scattering coefficient (lidar
497 ratio) for smoke particles of around 60-80 sr and associated IR/Visible color ratio of around 1.5-3. Using
498 reference stratospheric values of temperature and pressure around 200-210K and 80-100 hPa
499 respectively, we calculate a Rayleigh contribution to the scattering ratio of around 1.7-1.9E-4 $km^{-1}.sr^{-1}$
500 and using the 60-80 sr lidar ratio, we derive a 1.3-1.5 532 nm scattering ratio from the ACE

measurements of Figure 7b which is in good agreement with the modelled 1.4-1.6 values of Figure 6. This agreement between ACE measurements of Figure 6 and 7 suggests that present plume modeling is accurate for identifying particles at high latitudes.

5.4 Local impact of the smoke plume on stratospheric ozone

The DDU lidar was also used for measurements of ozone vertical profiles up to 2012. Such measurements are available on the 3rd of March, but not on the 1st of March. Figure 8a presents the lidar ozone profile measured on the same day, a few hours after the measurement of the aerosol profile. The dotted black line indicates the 3-year (2006-2008) average lidar ozone profile for this same period of the year. This background averaged profile agrees with a typical zonal mean climatology [Bencherif et al., 2011] for the relevant latitudinal range [75°S-85°S] which is indicated by the dotted red line. The interesting feature is the presence of a 1 km-thick enhanced ozone layer at about the altitude of the smoke layer.

However, similar ozone enhancements have been reported in smoke layers in previous studies. Fromm et al. [2005] studied a PyroCb injection of smoke to the stratosphere in August 1998 above Northwestern Canada using balloon profiles. They reported the first highly enhanced ozone concentration at the smoke altitude. These reports remain rare because simultaneous smoke and ozone measurements in the stratosphere are not common. It would be worthwhile to consider more cases to establish unequivocally a link between smoke and ozone enhancements in the stratosphere. It has been shown in tropospheric biomass burning plumes that ozone production can be expected and is observed [Pickering et al., 1996; Andreae et al., 2001] but at stratospheric altitudes, no clear process is identified to our knowledge to explain this positive correlation between ozone and smoke particles. Yu et al. [2019] used photochemistry modeling to assess the impact of smokes on O_3 on the Canadian 2017 fire event, only attributing negative anomalies observed by satellite to transport of air masses from the troposphere, with no in situ chemistry.

Figure 9 shows the ozone mixing ratio on the 395 K and 430 K isentropes from ERA-Interim. A filament of ozone-rich air from higher latitude appears to be lying close to DDU. It is possible that the ozone feature, which is mainly below and inside the smoke layer, could simply show the demarcation between air that has originated from further south (having higher ozone, and being below the smoke layer) from air that is more representative of the zonal average. Further studies combining measurements and chemistry-transport model on the air mass composition inside and outside the plume would be needed to state on this positive correlation because different mechanisms could lead to opposite ozone variations (like decrease from photolysis on water vapor and increase from CO concentrations). Besides, investigations using the observations like ACE or OSIRIS at high latitudes is difficult as the extinction coefficients associated to these aerosols are relatively small (compare with Figure 7).

6. Summary and concluding remarks

An event of stratospheric biomass burning aerosols was detected in the lower stratosphere on the coast of Antarctica using lidar measurements at the end of the Southern Hemisphere summer. Our investigations show that these aerosols originate from the 2009 Australian 'Black Saturday' smoke plume. From this detection, we develop a transport/microphysic modeling tool taking advantage of space-borne measurements to be a useful complement to the groundbased measurements in a region where instrumental capabilities are low as compared to lower latitudes. Due to this low instrumental coverage and fine optical signature of such events, we therefore highlight the underestimated occurrences of such polar detections in the many reported PyroCb events, and therefore link the PyroCb impacts to scientific questions more specific to high latitude regions.

Our global simulations of the microphysical/transport model indicated that following the February 7th Black Saturday event, particles reached the stratosphere within 2 days after the fire outbreak and crossed the tropical dynamical barriers down to the high latitudes in less than a week. Lidar measurements are routinely performed from the early days of March at the French Dumont d'Urville station, around one month after the fires in Australia. We identified a clear optical signature. An average scattering ratio slightly above 1.4 is identified at the 532nm wavelength, which is comparable to the optical response of moderate volcanic plume after several months of stratospheric transport.

A first step towards a more in-depth parametrization of the different particle types present in the UTLS has been developed and applied to this case study. The modeling approach allows for high resolution hemispheric transport of a smoke plume proxy to which optical properties are fit at the microphysical level to the optical properties measured by the CALIOP space-borne lidar. The dedicated MIMOSA-μφ model was run over a 5-month time period, as the overall global signature of the fire plume is reported up to June.

Without implementation of a full data assimilation scheme, this simulation is built on a 2-step procedure. A first spin-up step where the model grid is filled with particles, being essentially background sulfate aerosols with an initial carbonated smoke cluster, using the CALIOP 532nm SR as the variable controlling the evolution of the bin-resolved size distribution from its reference background parameters. This first step runs through the first month of the run time and leads to a realistic pattern of the global particle stratospheric load on the southern hemisphere. In the second step, the model runs on both a forced and free regime, considering the 50°S parallel as the latitude limit beyond which the advection is freely performed. After more than one month of long-range transport, our proxy of the smoke plume is found to be at a time and place globally consistent with the lidar measurements on both March the 1st and 3rd. This simulation highlights the opportunity for air masses coming from lower latitudes to deeply imprint the Antarctic stratosphere, as only some polar cloud types and similar transport of any strong volcanic plume would feature similar SR values. The quantitative assessment of the carbonated aerosol mass and smoke composition will need further microphysical investigations and many improvements on the model are necessary.

This work reports to our knowledge the first lidar identification of stratospheric smoke aerosols, the observed signature observed at the French Dumont d'Urville station originates from the 2009 wildfire event. We highlight the benefits of an efficient yet simple model-instrumental coupling. Accurate plume characterization can be made from a small sample of measurements and relatively simple modeling tools. Thus, we see three different outlines in this study: first, the scientific and confirmed pathway to a global impact (yet to be estimated) of long-range troposphere to stratosphere transport through pyroconvection and deep stratospheric transport for smoke. Second, the need for better characterization of the microphysical properties of such smoke, as their trapping above the Antarctic area is likely to have an impact on the ground level once deposited on ice shelves, especially over longer time scales. Third, the needed effort towards a better coupling of models and observations at the global scale. This can be achieved through assimilation of diagnostic variables such as the scattering ratio, especially when considering the overall success of space-borne lidar instruments and the need for maintaining routine lidar operations in polar stations.

In this study few compromises are made with the model grid size, resolution, and level of microphysical detail. This highlights the importance of dedicated data assimilation tools. Satellite measurements combined with global and regional models can be an efficient complementary data source to document transport of fine volcanic or biomass burning plumes, especially considering the 2019/2020 Australian wildfire event, which strength and amplitude is already acknowledged to be much greater than the 2009 event.

Acknowledgments and data availability

Operations on the Dumont D'Urville station are supported by the French Polar Institute (Institut polaire français Paul-Emile Victor), science project 209. This work was also performed within the EECLAT project (CNES-INSU). The lidar instrument is part of the NDACC international network and data are publicly available online at the NDACC/NOAA data archive (ftp://ftp.cpc.ncep.noaa.gov/ndacc/station/dumont/ames/). The Davis lidar observations and data analysis were supported by Australian Antarctic Science projects 737, 3140 and 4292 and these data are publically available through the Australian Antarctic Data Centre (http://aadc.aad.gov.au).

The MIMOSA transport model outputs are available online at the french ESPRI data archive :
https://cds-espri.ipsl.upmc.fr/etherTypo/index.php?id=1663&L=1).
Measurements from the ESA SCISAT-1/ACE instrument are available online at:
https://databace.scisat.ca/level2/
Measurements from the CALIPSO/CALIOP space-borne lidar are available online at:
https://www-calipso.larc.nasa.gov/tools/data_avail/

References

Adriani, A., P. Massoli, G. Di Donfrancesco, F. Cairo, M. L. Moriconi, and M. Snels (2004), Climatology of polar stratospheric clouds based on lidar observations from 1993 to 2001 over McMurdo Station, Antarctica, *J. Geophys. Res.*, 109, Z24211, doi:10.1029/2004JD004800.

Andreae, M. O., and P. Merlet, Emissions of trace gases and aerosols from biomass burning, Global Biogeochem. Cycles, 15, 955 – 966, 2001.

Alexander, S. P., A. R. Klekociuk and D. J. Murphy (2011), 'Rayleigh lidar observations of gravity wave activity in the winter upper stratosphere and lower mesosphere above Davis, Antarctica (69°S, 78°E), Journal of Geophysical Research, 116, D13109, doi:10.1029/2010JD015164.

635 Alexander, S. P., A. R. Klekociuk and D. J. Murphy (2011), 'Rayleigh lidar observations of gravity wave activity in the winter
636 upper stratosphere and lower mesosphere above Davis, Antarctica (69°S, 78°E), Journal of Geophysical Research, 116,
637 D13109, doi:10.1029/2010JD015164.

638 Arthern, R. J., D. P. Winebrenner, and D. G. Vaughan (2006), Antarctic snow accumulation mapped using polarization of 4.3-
639 cm wavelength microwave emission, J. Geophys. Res., 111, D06107, doi:10.1029/2004JD005667.

640 Bencherif H., El Amraoui L., Kirgis G., Leclair de Bellevue J., Hauchecorne A. (2011), Analysis of a rapid increase of stratospheric
641 ozone during late austral summer 2008 over Kerguelen (49.4° S, 70.3° E). Atmospheric Chemistry and Physics, European
642 Geosciences Union, 11 (1), pp.363-373. <10.5194/acp-11-363-2011>.

643 Bodhaine, B. A. (1995), Aerosol absorption measurements at Barrow,Mauna Loa and South Pole, J. Geophys. Res., 100, 8967–
644 8975.

645 Bullard J., M. Baddock, T. Bradwell T., J. Crusius, E. Darlington, D. Gaiero, S. Gassó, G. Gisladottir, R. Hodgkins, R. McCulloch,
646 C. McKenna-Neuman, T. Mockford, H. Stewart, T. Thorsteinsson (2016), High-latitude dust in the Earth system, Rev.
647 Geophys., 54, 447- 485, doi:10.1002/2016RG000518.

648 Bureau of Meteorology (BOM) (2009), Meteorological aspects of the 7 February 2009 Victorian fires, an overview. Bureau of
649 Meteorology report for the 2009 Victorian Bushfires Royal Commission, Bureau of Meteorology, Melbourne, Australia.

650 Burton, S.P., R.A. Ferrare, C.A. Hostetler, J.W. Hairl, R.R. Rogers, M.D. Obland, C.F. Butler, A.L. Cook, D.B. Harper and K.D.
651 Froyd, Aerosol classification using airborne High Spectral Resolution Lidar measurements – methodology and examples
652 (2012), Atmos. Meas. Tech., 5, 73–98, 2012, doi:10.5194/amt-5-73-2012.

653 Campbell. J.R., J.S. Reid, D.L. Westphal, J. Zhang, E.J. Hyer, and E.J. Welton (2010), CALIOP aerosol subset processing for global
654 aerosol transport model data assimilation, 2010, IEEE Journal of Selected Topics In Applied Earth Observations And
655 Remote Sensing, 3-2, 203-14. ISSN: 1939-1404.

656 Charlson, R. J., S. E. Schwartz, J. M. Hales, R. D. Cess, J. A. Coakley Jr., J. E. Hansen, and D. J. Hofmann (1992), Climate forcing
657 by anthropogenic aerosols, Science, 255, 423–430.

658 Chazette, P., C. David, J. Lefrère, S. Godin, J. Pelon, and G. Mégie (1995), Comparative lidar study of the optical, geometrical
659 and dynamical properties of the stratospheric post-volcanic aerosols following the eruption of El-Chichon and Mount
660 Pinatubo, J. Geophys. Res., 100(D11), 23,195–23,207, doi:10.1029/95JD02268.

661 Dahlkötter F., M. Gysel, D. Sauer, A. Minikin, R. Baumann, P. Seifert, A. Ansmann, M. Fromm, C. Voigt, and B.Weinzierl (2014),
662 The Pagami Creek smoke plume after long-range transport to the upper troposphere over Europe – aerosol properties
663 and black carbon mixing state, Atmos. Chem. Phys., 14, 6111-6137, doi:10.5194/acp-14-6111-2014.

664 David C., S. Bekki, S. Godin, and G. Mégie (1998), Polar stratospheric clouds climatology over Dumont d'Urville between 1989
665 and 1993 and the influence of volcanic aerosols on their formation, J. Geophys. Res., 103, 22,163-22,180.

666 David C., S. Bekki, N. Berdunov, M. Marchand, and G. Mégie (2005), Classification and scales of Antarctic Polar Stratospheric
667 Clouds using wavelet decomposition, J. Atm. Solar-Terrestr. Physics, 67, 293-300.

668 David C., A. Haefele, P. Keckhut, M. Marchand, J. Jumelet, T. Leblanc, C. Cenac, C. Laqui, J. Porteneuve, M. Haefflin, Y.
669 Courcoux, M. Snels, M. Viterbini, and M. Quatrevalet (2012) Evaluation of stratospheric ozone, temperature, and aerosol
670 profiles from the LOANA lidar in Antarctica, Polar Science, doi: 10.1016/j.polar.2012.07.001.

671 Dodion, J., et al. (2007), Cloud detection in the upper troposphere-lower stratosphere region via ACE imagers: A qualitative
672 study, J. Geophys. Res., 112, D03208, doi:10.1029/2006JD007160.

673 Dowdy, A. J., M. D. Fromm, and N. McCarthy (2017), Pyrocumulonimbus lightning and fire ignition on Black Saturday in
674 southeast Australia, J. Geophys. Res. Atmos., 122, doi:10.1002/2017JD026577.

675 Edwards, D. P., L. K. Emmons, J. C. Gille, A. Chu, J.-L. Attié, L. Giglio, S. W. Wood, J. Haywood, M. N. Deeter, S. T. Massie, D. C.
676 Ziskin, and J. R. Drummond (2006), Satellite Observed Pollution from Southern Hemisphere Biomass Burning, J. Geophys.
677 Res., 111, D14312, doi:10.1029/2005JD006655.

678 Evangelista, H., J. Maldonado, R.H.M. Godoi, E.B. Pereira, D. Koch, K. Tanizaki-Fonseca, R. Van Grieken, M. Sampaio, A. Setzer,
679 A. Alencar, and S.C. Gonçalves (2007), Sources and transport of urban and biomass burning aerosol black carbon at the
680 South-West Atlantic coast, J. Atmos. Chem., 56, 225–238.

681 Fernald, F. G. (1984), Analysis of atmospheric lidar observations: some comments, Appl. Opt., 23, 652–653.

682 Fiebig, M., C. R. Lunder, and A. Stohl (2009), Tracing biomass burning aerosol from South America to Troll research station,
683 Antarctica, Geophys. Res. Lett., 36, L14815, doi:10.1029/2009GL038531.

684 Field, R. D., M. Luo, M. Fromm, A. Voulgarakis, S. Mangeon, and J. Worden (2016), Simulating the Black Saturday 2009 smoke
685 plume with an interactive composition-climate model: Sensitivity to emissions amount, timing, and injection height, J.
686 Geophys. Res. Atmos., 121, 4296–4316, doi:10.1002/2015JD024343.

687 Forster, C., A. Stohl, and P. Seibert (2007), Parameterization of convective transport in a Lagrangian particle dispersion model
688 and its evaluation, J. Appl. Meteorol. Climatol., 46, 403– 422.

689 Fromm, M., J. Alfred, K. Hoppel, J. Hornstein, R. Bevilacqua, E. Shettle, R. Servranckx, Z. Li, and B. Stocks (2000), Observations
690 of boreal forest fire smoke in the stratosphere by POAM III, SAGE II, and lidar in 1998, Geophys. Res. Lett., 27, 1407–
691 1410.

692 Fromm, M. D., and R. Servranckx (2003), Transport of forest fire smoke above the tropopause by supercell convection,
693 Geophys. Res. Lett., 30(10), 1542, doi:10.1029/2002GL016820.

694 Fromm, M., R. Bevilacqua, R. Servranckx, J. Rosen, J. P. Thayer, J. Herman, and D. Larko (2005) Pyro-cumulonimbus injection
695 of smoke to the stratosphere: Observations and impact of a super blowup in northwestern Canada on 3–4 August 1998,
696 J. Geophys. Res., 110, D08205, doi:10.1029/2004jd005350.

697 Fromm M., O. Torres, D. Diner, D. Lindsey, B. Vant Hull, R. Servranckx, E. P. Shettle, and Z. Li (2008), Stratospheric impact of
698 the Chisholm pyrocumulonimbus eruption 1. Earth-viewing satellite perspective, J. Geophys. Res., 113, D08202,
699 doi:10.1029/2007JD009153.

700 Fromm, M., D. T. Lindsey, R. Servrqanckx, G. Yue, T. Trickl, R. Sica, P. Douget, and S. Godin-Beekmann (2010), The untold story
701 of pyrocumulonimbus, Bull. Am. Meteorol. Soc., 91, 1193–1209, doi:10.1175/2010BAMS3004.1.

702 Gassó, S., A. Stein, F. Marino, E. Castellano, R. Udisti, and J. Ceratto (2010), A combined observational and modeling approach
703 to study modern dust transport from the Patagonia desert to East Antarctica, Atmos. Chem. Phys., 10, 8287-
704 8303, https://doi.org/10.5194/acp-10-8287-2010.

705 Gauss M., G. Myhre, G. Pitari, M. J. Prather,I. S. A. Isaksen,1 T. K. Berntsen, G. P. Brasseur, F. J. Dentener, R. G. Derwent, D. A.
706 Hauglustaine, L. W. Horowitz, D. J. Jacob, M. Johnson, K. S. Law, L. J. Mickley, J.-F. Müller,P.-H. Plantevin, J. A. Pyle, H. L.
707 Rogers, D. S. Stevenson, J. K. Sundet, M. van Weele, and O. Wild (2003), Radiative forcing in the 21st century due to ozone
708 changes in the troposphere and the lower stratosphere, J. Geophys. Res., 108(D9), 4292, doi:10.1029/2002JD002624.

709 Gilbert, K.L., Turnbull, D.N., Walker, K.A., Boone, C.D., McLeod, S.D., Butler, M., Skelton, R., Bernath, P.F., Chateauneuf, F.,
710 Soucy, (2007) M.-A. The On-Board Imagers for the Canadian ACE SCISAT-I Mission. J. *Geophys. Res.* 112,
711 doi:10.1029/2006JD007714.

712 Glatthor, N., M. Höpfner, K. Semeniuk, A. Lupu, P. I. Palmer, J. C. McConnell, J. W. Kaminski, T. V. Clarmann, G. P. Stiller, B.
713 Funke, and S. Kellmann (2013), The Australian bushfires of February 2009: MIPAS observations and GEM-AQ model
714 results, Atmos. Chem. Phys., 13(3),1637–1658.

715 Hauchecorne, A., S. Godin, M. Marchand, B. Heese, and C. Souprayen (2001), Quantification of the transport of chemical
716 constituents from the polar vortex to midlatitudes in the lower stratosphere using the high-resolution advection model
717 MIMOSA and effective diffusivity, J. Geophys. Res., 107(D20), 8289, doi:10.1029/2001JD000491.

718 Heese, B., S. Godin, and A. Hauchecorne (2001), Forecast and simulation of stratospheric ozone filaments: A validation of a
719 high-resolution PV advection model by airborne ozone lidar measurements in winter 1998–1999, J. Geophys. Res., 20011–
720 20024.

721 Ito, T., Y. Morita, and Y. Iwasaka (1986), Balloon observations of aerosols in the Antarctic troposphere and stratosphere,
722 Tellus, Ser. B, 38, 214–222.

723 Jost, H. J., K. Drdla, A. Stohl, L. Pfister, M. Loewenstein, J. P. Lopez, P. K. Hudson, D. M. Murphy, D. J. Cziczo, M. Fromm, T. P.
724 Bui, J. Dean-Day, C. Gerbig, C., M. J. Mahoney, E. C. Richard, N. Spichtinger, J. V. Pittman, E. M. Weinstock, J. C. Wilson,
725 and I. Xueref (2004), In-situ observations of mid-latitude forest fire plumes deep in the stratosphere, Geophys. Res. Lett.,
726 31,L11101,doi:10.1029/2003gl019253.

727 Jumelet J., S. Bekki, P. Seifert, N. Montoux, J.P. Vernier, and J. Pelon (2009), Microphysical modeling of a mid-latitude Polar
728 stratospheric cloud event: Comparisons against multiwavelength ground-based and space-borne lidar data, J. Geophys.
729 Res., doi:2009JD011776.

730 Kablick G., M. Fromm , S. Miller, P. Partain, D. Peterson, S. Lee, Y. Zhang, A. Lambert and Z. Li (2018), The Great Slave Lake
731 PyroCb of 5 August 2014: Observations, Simulations, Comparisons With Regular Convection, and Impact on UTLS Water
732 Vapor, j.geophys.research, 123, 21, 12,332-12,352, doi.org/10.1029/2018JD028965

733 Klett J.D. (1981), Stable analytical inversion solution for processing lidar returns, Appl. Opt., 20, 2.

734 Klett J.D. (1985), Lidar inversion with variable backscatter/extinction ratios, Appl. Opt., 24, 1638, 1985.

735 Kottmeier, C., and B. Fay (1998), Trajectories in the Antarctic lower troposphere, J. Geophys. Res., 103, 10,947–10,959.

736 Lachlan-Cope, T. (2010), Antarctic clouds, Polar Res., 29, 150–158, doi:10.1111/j.1751-8369.2010.00148.x.

737 Larsen N. (2000), Polar stratospheric clouds microphysical and optical models, Danish Meteorological Institute, Scientific
738 report, 00-06, 85 pp.

739 Liou, K. N. (1986), Influence of cirrus clouds on weather and climate processes: A global perspective, Mon. Weather Rev., 114,
740 1167–1199, doi:10.1175/1520-0493.

741 Liu, D., J. Allan, J. Whitehead, D. Young, M. Flynn, H. Coe, G. McFiggans, Z. L. Fleming, and B. Bandy (2013), Ambient black
742 carbon particle hygroscopic properties controlled by mixing state and composition, Atmos. Chem. Phys., 13, 2015–2029,
743 doi:10.5194/acp-13-2015-2013.

744 Livesey, N. J., M. D. Fromm, J. W. Waters, G. L. Manney, M. L. Santee, and W. G. Read (2004), Enhancements in lower
745 stratospheric CH3CN observed by the Upper Atmosphere Research Satellite Microwave Limb Sounder following boreal
746 forest fires, J. Geophys. Res., 109, D06308, doi:10.1029/2003JD004055.

747 McConnell, J. R., A. J. Aristarain, J. R. Banta, P. R. Edwards, and J. C.Simões (2007), 20th-century doubling in dust archived in
748 an Antarctic Peninsula ice core parallels climate change and desertification in South America, Proc. Natl. Acad. Sci. U. S.
749 A., 104, 5743– 5748.

750 Mischenko, M.I., L. Liu, B. Cairns, and D.W. Mackowski (2014) Optics of water cloud droplets mixed with black-carbon
751 aerosols, Opt Letters, 39, 2607-2610.

752 Penner, J. E., Andreae, M., Annegarn, H., et al. Aerosols: Their direct and indirect effects, in Climate Change 2001 The Scientific
753 Basis, pp. 289–348, Cambridge Univ. Press, New York.

754 Pereira, E. B., H. Evangelista, K. C. D. Pereira, I. F. A. Cavalcanti, and A.W. Setzer (2006), Apportionment of black carbon in the
755 South Shetland Islands, Antarctic Peninsula, J. Geophys. Res., 111, D03303, doi:10.1029/2005JD006086.

756 Peterson, D.A., E.J. Hyer, J.R. Campbell, M.D. Fromm, J.W. Hair, C.F. Butler, and M.A. Fenn (2015), The 2013 Rim Fire:
757 Implications for Predicting Extreme Fire Spread, Pyroconvection, and Smoke Emissions, Bull. Amer. Meteor. Soc., 96-2,
758 229–247, doi.org/10.1175/BAMS-D-14-00060.1.

759 Peterson, D.A., J.R. Campbell, E.J. Hyer, M.D. Fromm, G.P. Kablick, J.H. Cossuth, and M.T. Deland (2018), Wildfire-driven
760 thunderstorms cause a volcano-like stratospheric injection of smoke., npj Clim Atmos Sci 1, 30. doi.org/10.1038/s41612-
761 018-0039-3.

762 Pickering, K. E., Thompson, A. M., Wang, Y., et al. (1996), Convective transport of biomass burning emissions over Brazil during
763 TRACE-A, J. Geophys. Res., 101, 23 993–24 012.

764 Pinnick R.G., J.M. Rosen, and D.J. Hofmann (1976), Stratospheric aerosol measurements III: Optical model calculations,
765 J. Atmos. Sc., 33, 304-314.

766 Pumphrey, H. C., Santee, M. L., Livesey, N. J., Schwartz, M. J., and Read, W. G. (2011): Microwave Limb Sounder observations
767 of biomass-burning products from the Australian bush fires of February 2009, Atmos. Chem. Phys., 11, 6285-6296,
768 doi:10.5194/acp-11-6285-2011.

769 Randles, C. A., L. M. Russell, and V. Ramaswamy (2004), Hygroscopic and optical properties of organic sea salt aerosol and
770 consequences for climate forcing, Geophys. Res. Lett., 31, L16108, doi:10.1029/2004GL020628.

771 Ramanathan, V., R. D. Cess, E. F. Harrison, P. Minnis, B. R. Barkstrom, E. Ahmad, and D. Hartman (1989), Cloud-radiative
772 forcing and climate: Results from the Earth Radiation Budget Experiment, Science, 243, 57–63,
773 doi:10.1126/science.243.4887.57.

774 Reeder, M. J., T. Spengler, and R. Musgrave (2015), Rossby waves, extreme fronts, and wildfires in southeastern Australia,
775 Geophys. Res. Lett.,42, 2015–2023, doi:10.1002/2015GL063125.

776 Ridley, D. A., et al. (2014), Total volcanic stratospheric aerosol optical depths and implications for global climate change,
777 Geophys. Res. Lett., 41, 7763–7769, doi:10.1002/2014GL061541.

778 Scarnato, B.V., S. China, K. Nielsen, and C. Mazzoleni (2015) Perturbations of the optical properties of mineal dust particles
779 by mixing with black carbon: a numerical simulation study, Atmos. Chem. Phys., 15, 6913-6928 doi:10.5194/acp-15-6913-
780 2015.

781 Sekiyama T.T., T. Y. Tanaka , A. Shimizu , and T. Miyoshi (2010), Data assimilation of CALIPSO aerosol observations , Atmos.
782 Chem. Phys., 10, 39–49.

783 Siddaway J. M., and S. V. Petelina (2011), Transport and evolution of the 2009 Australian Black Saturday bushfire smoke in
784 the lower stratosphere observed by OSIRIS on Odin, J. Geophys. Res., 116, D06203, doi:10.1029/2010JD015162.

785 Siebert, J., C. Timmis, G. Vaughan, and K. Fricke (2000), A strange cloud in the Arctic summer 1998 above Esrange (68N),
786 Sweden, Ann. Geophys., 18, 505– 509.

787 Sigl, M., J.R. McConnell, M. Toohey, M. Curran, S.B. Das, R. Edwards, E. Isaksson, K. Kawamura, S. Kipfstuhl, K. Krueger, L.
788 Layman, O.J. Maselli, Y. Motizuki, H. Motoyama, D.R. Pasteris, and M. Severi (2014) Insights from Antarctica on volcanic
789 forcing during the Common Era., Nature Climate Change, 4, 693–697, doi:10.1038/nclimate2293.

790 Smith A.J.A., and R.G. Grainger (2014), Simplifying the calculation of light scattering properties for black carbon fractal
791 aggregates, Atmos. Chem. Phys., 14, 7825-783.

792 Spinhirne, J. D., S. P. Palm, and W. D. Hart (2005), Antarctica cloud cover for October 2003 from GLAS satellite lidar profiling,
793 Geophys. Res. Lett., 32, L22S05, doi:10.1029/2005GL023782.

794 Stohl A., and H. Sodemann (2010), Characteristics of atmospheric transport into the Antarctic troposphere, J. Geophys. Res.,
795 115, D02305, doi:10.1029/2009JD012536.

796 Thomason, L. and Peter, T. (2006), Assessment of Stratospheric Aerosol Properties, Tech. Rep. WMO-TD No. 1295, WCRP
797 Series Report No. 124, SPARC Report No. 4, Berrieres le Buisson Cedex.

798 Tomasi C., V. Vitale, A. Lupi, C. Di Carmine, M. Campanelli, A. Herber, R. Treffeisen, R. S. Stone, E. Andrews, S. Sharma, V.
799 Radionov, W. von Hoyningen-Huene, K. Stebel, G. H. Hansen, C. L. Myhre, C. Wehrli, V. Aaltonen, H. Lihavainen, A.
800 Virkkula, R. Hillamo, J. Ström, C. Toledano, V. E. Cachorro, P. Ortiz, A. M. de Frutos, S. Blindheim, M. Frioud, M. Gausa, T.
801 Zielinski, T. Petelski, and T. Yamanouchi (2007), Aerosols in polar regions: A historical overview based on optical depth
802 and in situ observations, J.Geophys. Res., 112, D16205, doi:10.1029/2007JD008432.

803 Tosca, M. G., D. J. Diner, M. J. Garay, and O. V. Kalashnikova (2015), Human-caused fires limit convection in tropical Africa:
804 First temporal observations and attribution, Geophys. Res. Lett., 42, 6492–6501, doi:10.1002/2015GL065063.

805 Tupper, A., J. S. Oswalt, and D. Rosenfeld (2005), Satellite and radar analysis of the volcanic-cumulonimbi at Mount Pinatubo,
806 Philippines, 1991, J. Geophys. Res., 110, D09204, doi:10.1029/2004JD005499.

807 Vernier, J.-P., et al. (2011a), Major influence of tropical volcanic eruptions on the stratospheric aerosol layer during the last
808 decade, Geophys. Res. Lett., 38, L12807, doi:10.1029/2011GL047563.

809 Vernier, J.-P., J.-P. Pommereau, L. W. Thomason, J. Pelon, A. Garnier, T. Deshler, J. Jumelet, and J.K. Nielsen (2011c)
810 Overshooting of clean tropospheric air in the tropical lower stratosphere as seen by the CALIPSO lidar, Atmos. Chem.
811 Phys., 11, 9683–9696, doi:10.5194/acp-11-9683-2011.

812 Waibel, A. E., H. Fischer, F. G. Wienhold, P. C. Siegmund, B. Lee, J. Ström, J. Lelieveld, and P. J. Crutzen (1999), Highly elevated
813 carbon monoxide concentrations in the upper troposphere and lowermost stratosphere at northern midlatitudes during
814 the STREAM II summer campaign in 1994, Chemosphere Global Change Sci., 1, 233– 248.

815 Wang, P. K. (2003), Moisture plumes above thunderstorm anvils and their contributions to cross-tropopause transport of
816 water vapor in midlatitudes, J. Geophys. Res., 108(D6), 4194, doi:10.1029/2002JD002581.

817 Wang, Z., G. M. Heymsfield, L. Li, and A. J. Heymsfield (2005), Retrieving optically thick ice cloud microphysical properties by
818 using airborne dual-wavelength radar measurements, J. Geophys. Res., 110, D19201, doi:10.1029/2005JD005969.

819 Weller, R., A. Minikin, A. Petzold, D. Wagenbach, D., and G. König-Langlo, Characterization of long-term and seasonal
820 variations of black carbon (BC) concentrations at Neumayer (2013), Antarctica, Atmos. Chem. Phys., 13, 1579-
821 1590, doi.org/10.5194/acp-13-1579-2013.

822 Winker, D. M., et al. (2010), The CALIPSO mission: A global 3D view of aerosols and clouds, Bull. Am. Meteorol. Soc., 91, 1211–
823 1229, doi:10.1175/2010BAMS3009.1.

824 Wolff, E. W., and D. A. Peel (1985), The record of global pollution in polar snow and ice, Nature, 313, 535– 540.

825 World Meteorological Organization (WMO) (2018), Scientific Assessment of Ozone Depletion: 2018, Global Ozone Reasearch
826 and Monitoring Project, Rep. 58, 590pp., Geneva, Switzerland.

827 Yasunari, T. J., R. D. Koster, K.-M. Lau, T. Aoki, Y. C. Sud, T. Yamazaki, H. Motoyoshi, and Y. Kodama (2011), Influence of dust
828 and black carbon on the snow albedo in the NASA Goddard Earth Observing System version 5 land surface model, J.
829 Geophys. Res., 116, D02210, doi:10.1029/2010JD014861.

830 Yu, P., O. B. Toon, C. G. Bardeen, Y. Zhu, K. H. Rosenlof, R. W. Portmann, T. D. Thornberry, R.-S. Gao, S. M. Davis, E. T. Wolf, J.
831 de Gouw, D. A. Peterson, M. D. Fromm. and A. Robock (2019), Black carbon lofts wildfire smoke high into the stratosphere
832 to form a persistent plume - Science 365 (6453), 587-590, doi: 10.1126/science.aax1748.

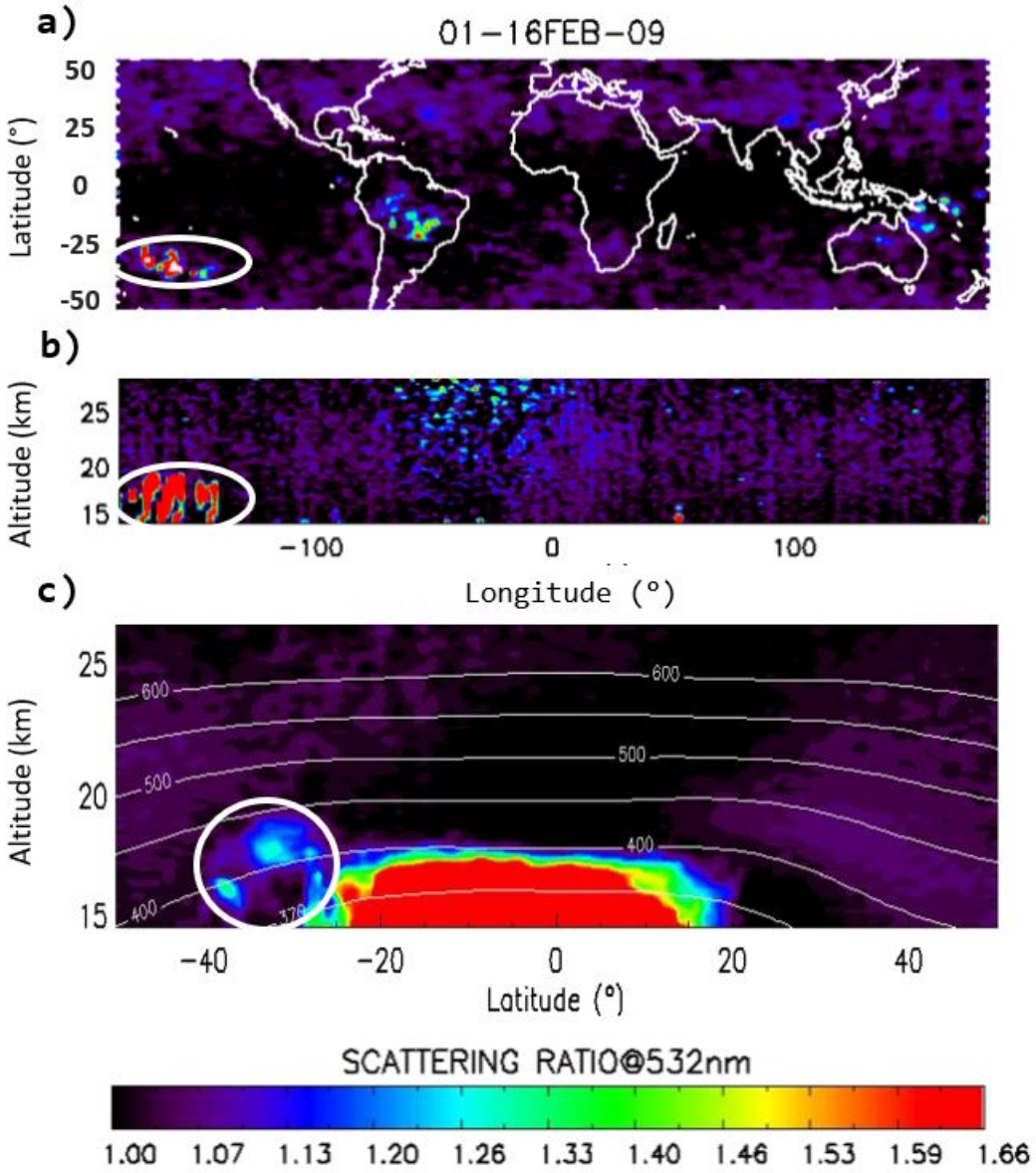

Fig. 1. 532nm CALIOP Scattering Ratio in the first 16 days of February plotted as longitude vs latitude, 15-20 km average (a), longitude vs altitude, averaged in the -25° to -50° latitudinal band (b), and latitude vs altitude (c). The smoke plume cluster is encircled in white and is clearly separated from the global tropospheric cloud signature. Contours of constant potential temperature (K) are shown.

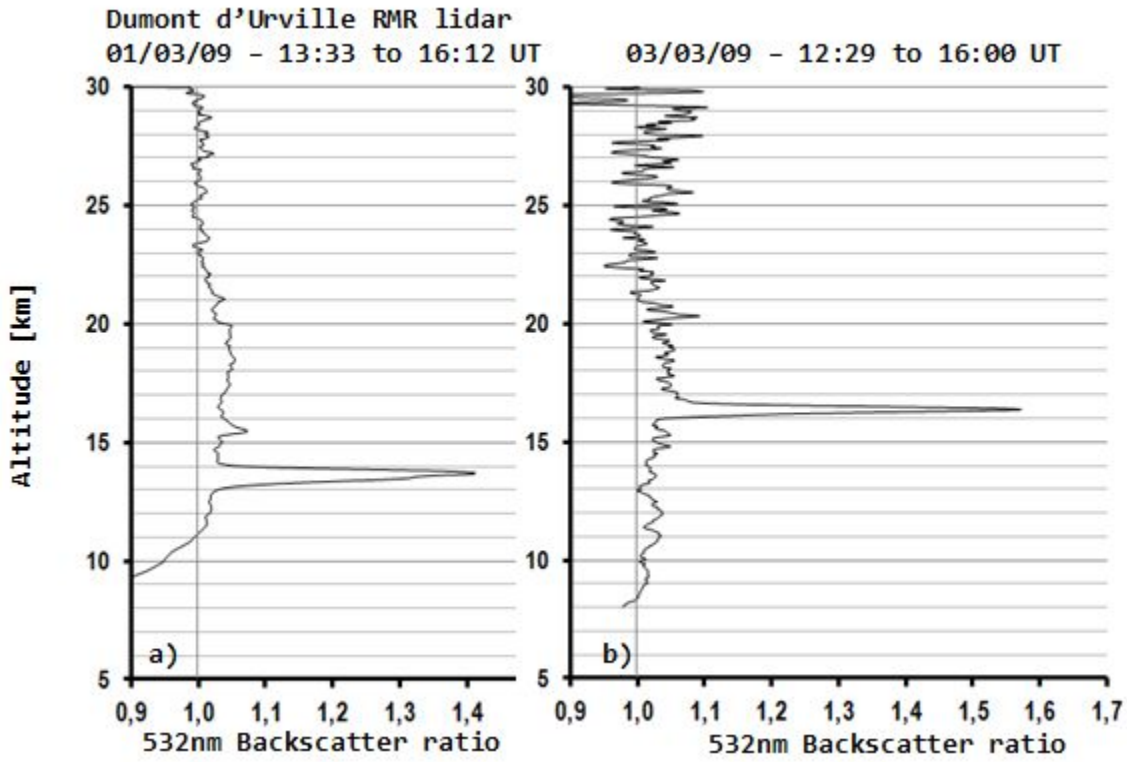

841
842
843 **Fig. 2.** Dumont d'Urville 532nm Scattering Ratio on March 1st (a), and 3rd (b) with smoke layers
844 respectively visible at 13.5 km and 16.4 km.
845
846

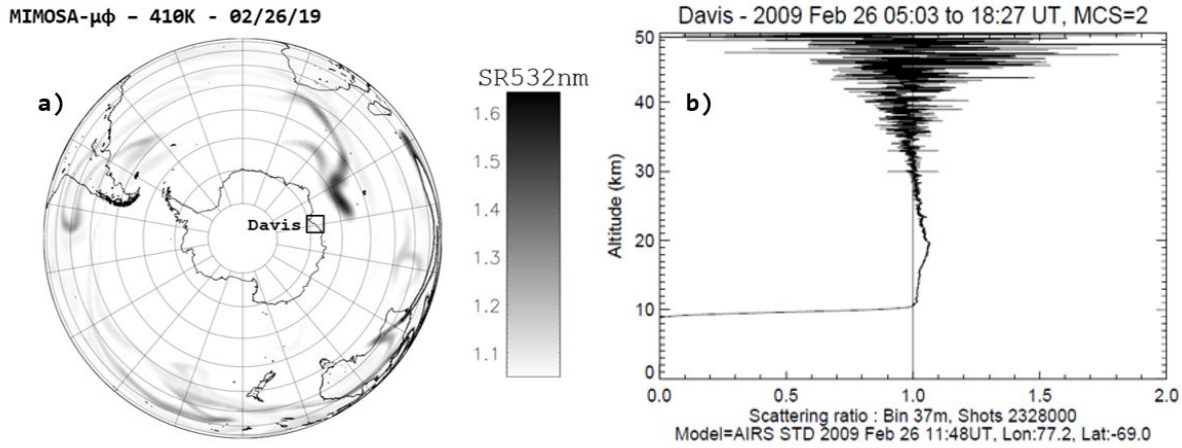

847
848 **Fig. 3.** (a) Model-simulated 532nm Scattering Ratio on February 26th. (b) 532nm lidar profile
849 acquired at Davis Station.

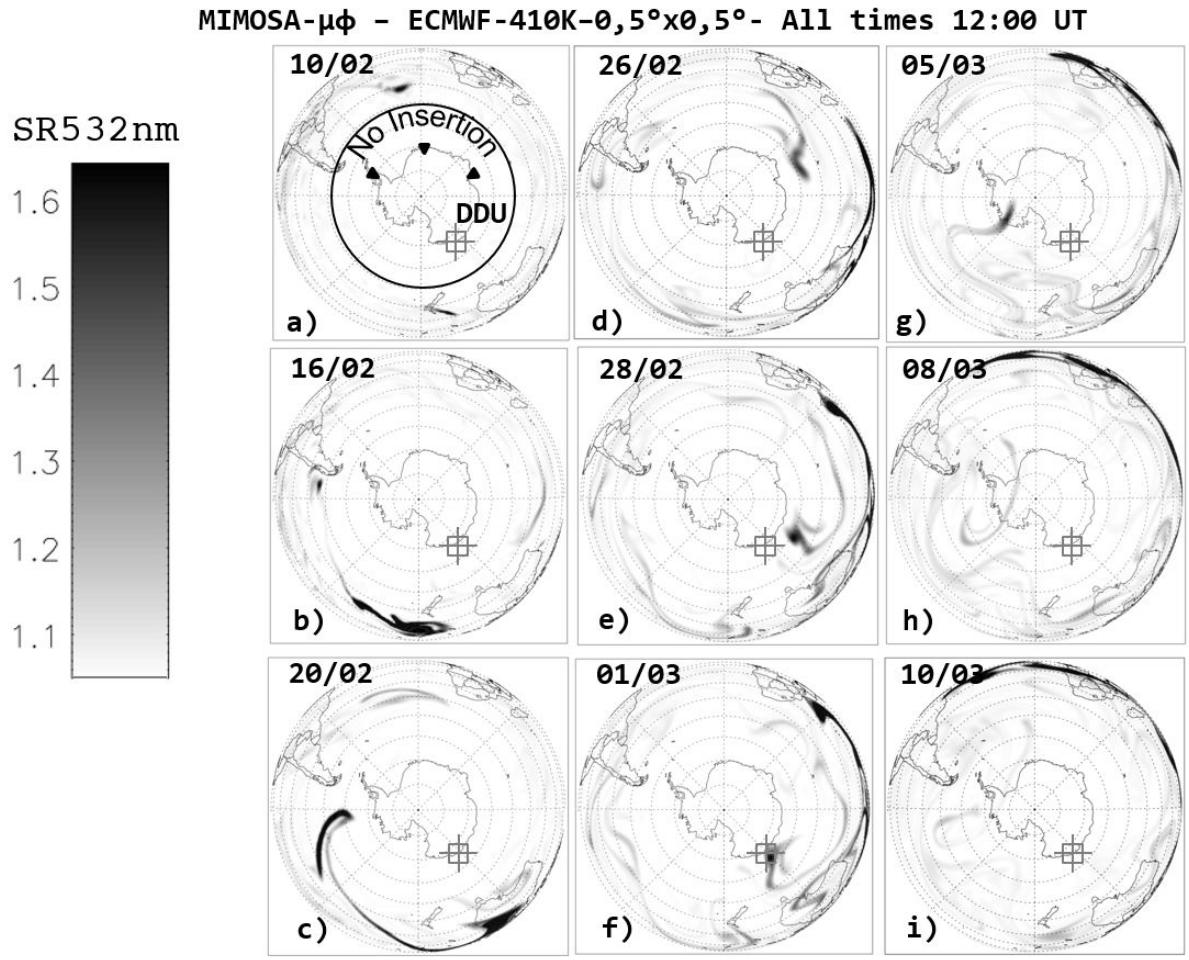

Fig. 4. 532nm MIMOSA-μφ SR calculations from February 10th to March 10th. Spatial resolution is 0.5°x0.5° and the potential temperature level is 410 K. CALIOP SR is integrated only up to the 16th of February and in the (-50°;50°) latitudinal range. The location of Dumont d'Urville station is indicated by the square.

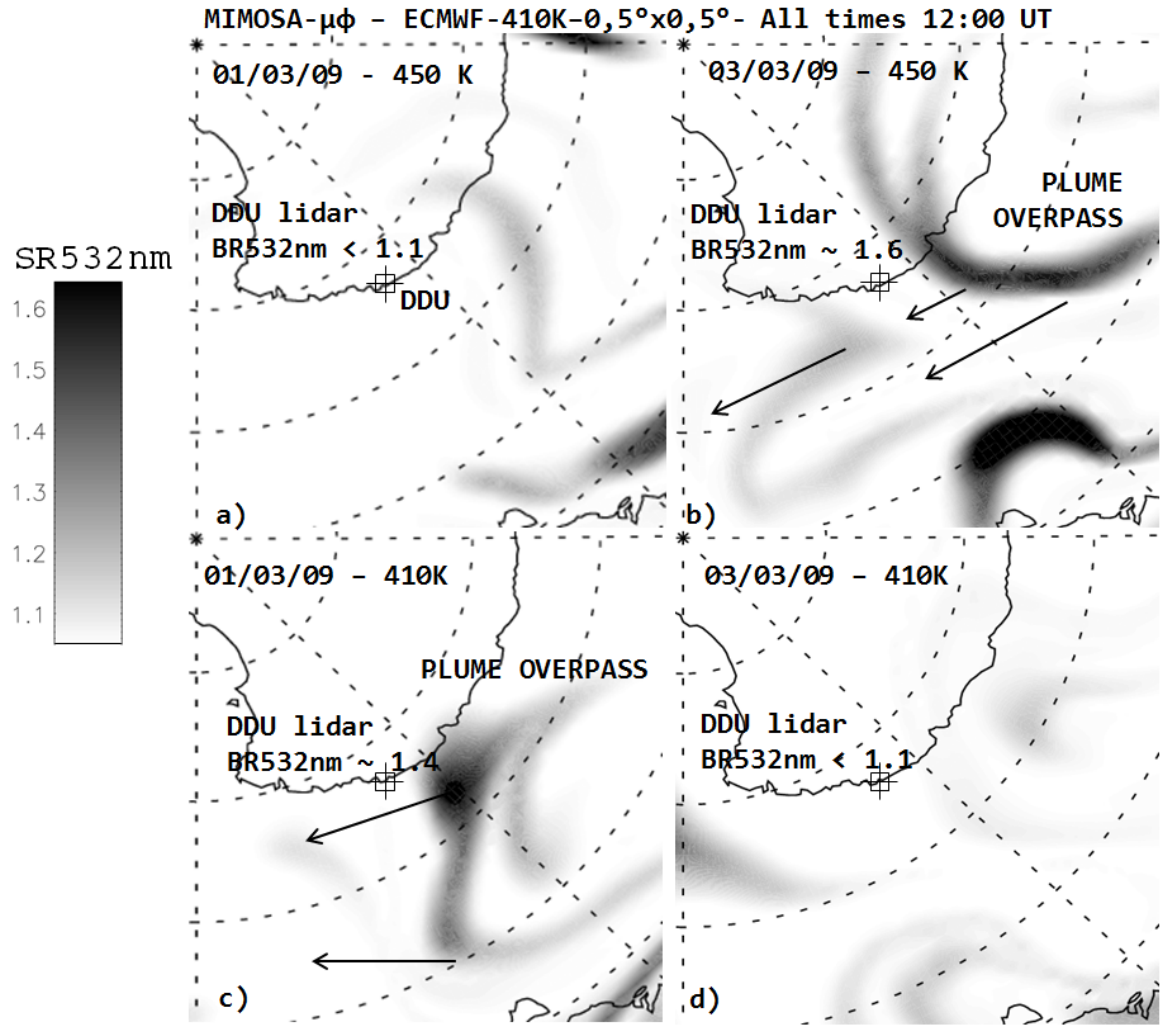

Fig. 5. 532nm MIMOSA-μφ Scattering Ratio calculations and detailed outputs above the vicinity of DDU on March 1st at 450 K (a), 410 K (c) potential temperature levels and March 3rd at 450 K (b), 410 K (d) potential temperature levels. Plume overpass is detected in Figure 4b and 4c consistently with lidar detections in Figure 1.

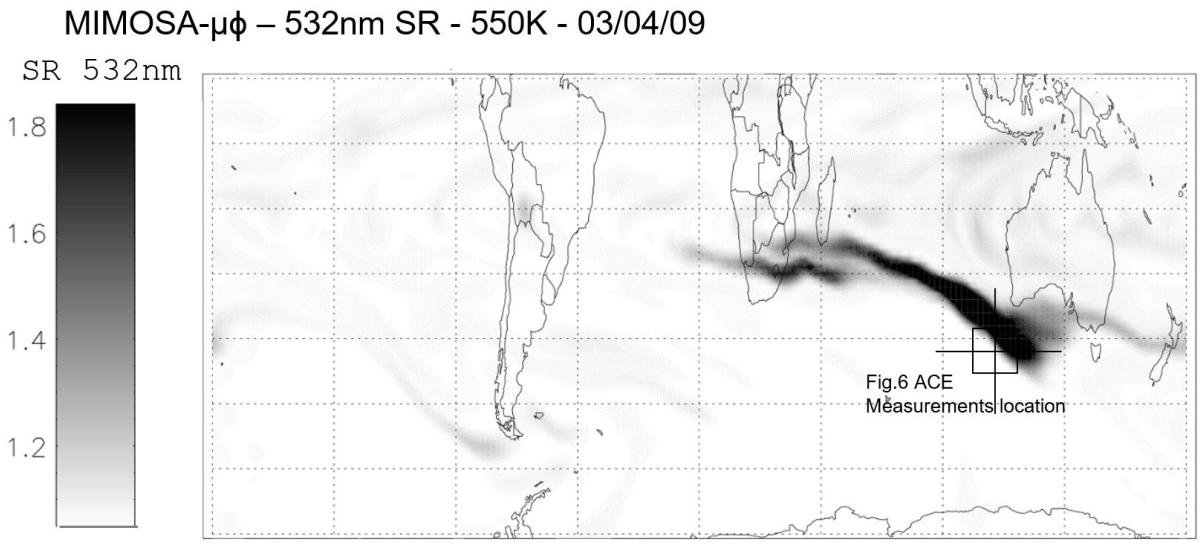

Fig. 6. 532nm MIMOSA-μφ SR calculations on March 4th (b). Crosshairs locate the ACE measurements displayed in Figure 7.

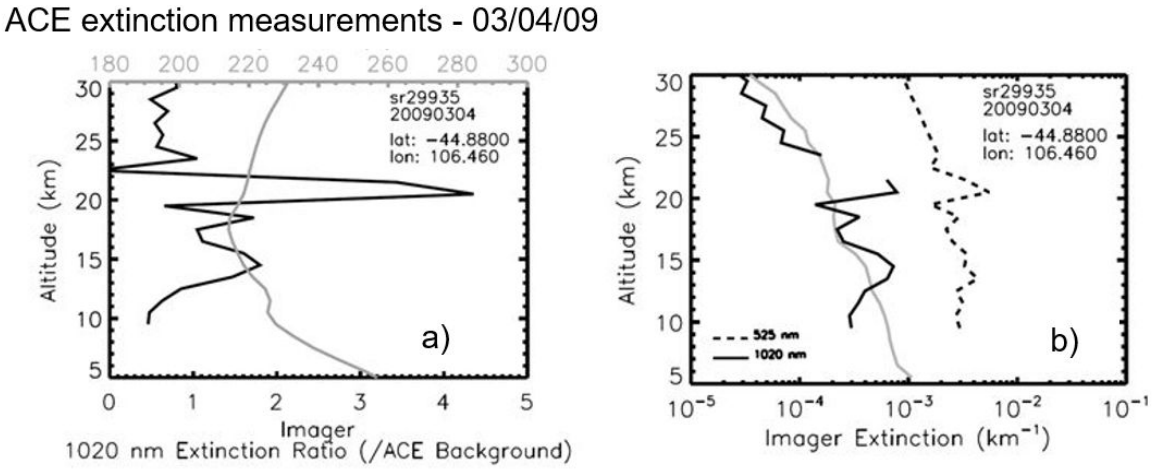

Fig. 7. Visible and Near Infra Red ACE imager measurements on March 3rd. (a) Extinction ratio is reported as compared to the ACE reference background. Imager extinction is in (b).

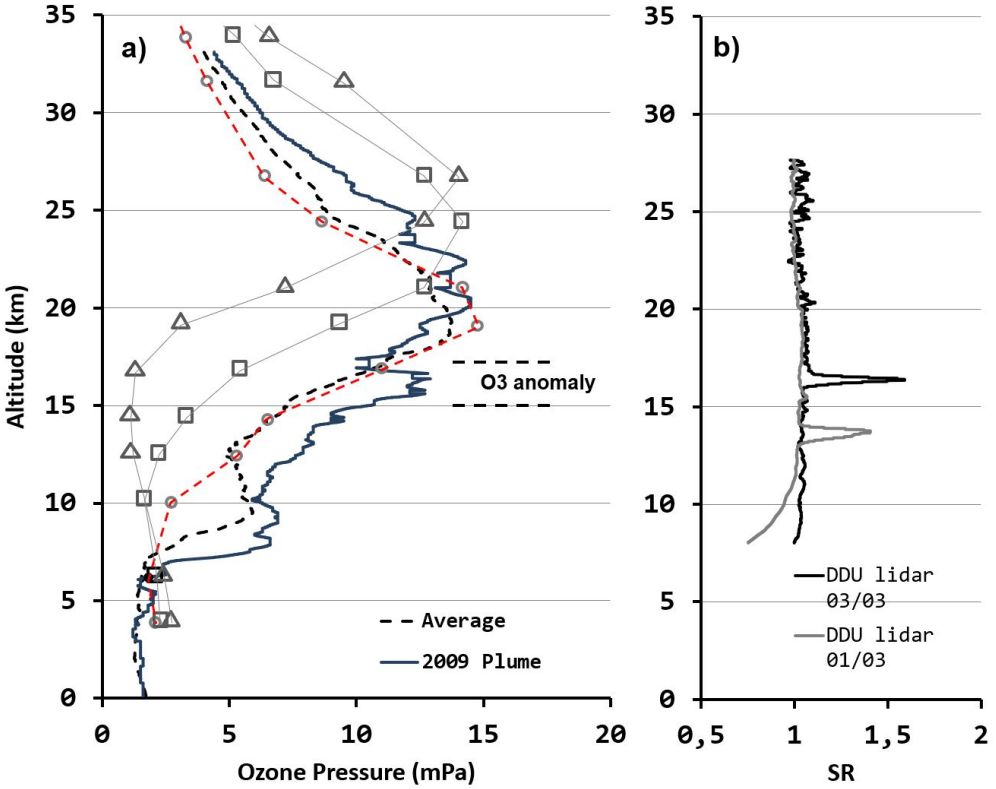

Fig. 8. (a) DDU Ozone lidar measurements as a vertical pressure profile on March 1st 2009 (blue line), together with a 3-year average at the same period (black dotted line) and latitudinal typical climatology: Triangle, square and circle marked lines refer to ozone profiles recorded from balloon sondes on 2008 at the Kerguelen Islands respectively on the [15°S-25°S], [45°S-55°S] and [75°S-85°S] latitudinal bands [Bencherif et al., 2011]. Excess ozone concentration is detected at the smoke altitude range above 15 km. For reference, aerosol lidar profiles are reported in (b).

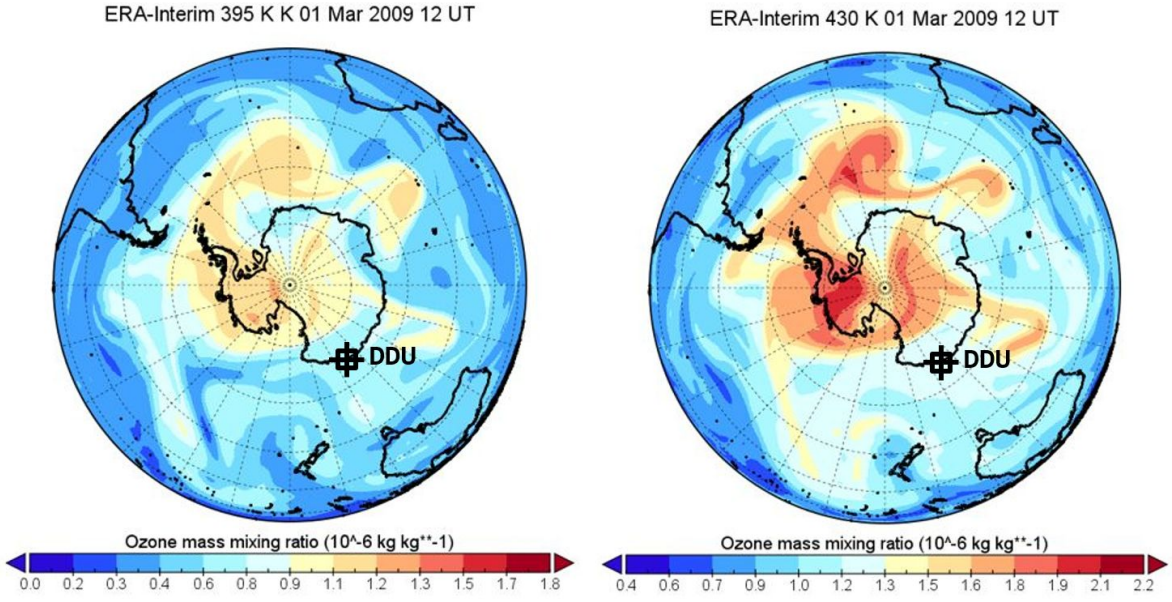

Fig. 9. Ozone mass mixing ratio from ERA-Interim at 12:00 UT on 01 March 2009 on the isentropic surfaces of (left) 395 K and (right) 430 K.